

Near-infrared spectro-interferometry of three OH/IR Stars with the VLT/AMBER instrument [★] (Research Note)

A. E. Ruiz-Velasco^{1,2}, M. Wittkowski¹, A. Wachter², K.-P. Schröder², and T. Driebe^{3,4}

¹ ESO, Karl-Schwarzschild-Str. 2, 85748 Garching bei München, Germany, e-mail: alma@astro.ugto.mx

² Departamento de Astronomía, Universidad de Guanajuato. Apartado Postal 144, 36000 Guanajuato, Mexico.

³ Max-Planck-Institut für Radioastronomie, Auf dem Hügel 69, 53121 Bonn, Germany

⁴ German Aerospace Center, Space Agency, Königswinterer-Straße 522-524, D-53227 Bonn, Germany

Received ...; accepted ...

ABSTRACT

Aims. We investigate the molecular and dusty environment of OH/IR stars in order to characterize the mass-loss process during the tip-AGB superwind phase.

Methods. Employing the AMBER instrument at the VLT Interferometer we obtained near-infrared *H*- and *K*-band spectro-interferometric observations of the three OH/IR stars IRAS 13479-5436, IRAS 14086-6907 and IRAS 17020-5254 with a spectral resolution of about 35. We use a two-component geometrical model, consisting of a uniform disk and a Gaussian disk, to obtain characteristic angular sizes of the central stellar sources and their dust envelopes, as well as the flux ratios between these components.

Results. Angular uniform disk diameters of the three central components of the objects above have values between 3.2 mas and 5.4 mas. For their dust envelopes, we find FWHM values between 17.1 mas and 25.2 mas. The three objects show significantly different flux contributions of the shells to the total near-IR flux of 61%, 38%, and 16% for IRAS 13479-5436, IRAS 14086-6907, and IRAS 17020-5254, respectively. According to distance estimates from the literature, the central stellar components have radii between 900 R_{\odot} and 1400 R_{\odot} , while their dust envelopes reach FWHM values between 9000 R_{\odot} and 13000 R_{\odot} . The visibility functions of all three sources exhibit wavelength variations that resemble those of earlier VLT/AMBER observations of semi-regular and Mira variable AGB stars. These are interpreted as characteristic of atmospheric molecular layers lying above the photosphere.

Conclusions. The derived characteristic sizes of both, the central stellar atmospheres and dust envelopes are consistent with the canonical properties of OH/IR stars. The spectral visibility variations resemble those of other AGB stars and indicate the presence of molecular layers, confirming that these are a common phenomenon among AGB stars of very different luminosities and mass-loss rates, alike. We also find that the dust envelopes have a clearly larger optical depth than those known for Mira stars. We interpret this as an expected result of the “superwind” phase, the final 10 000 to 30 000 years of AGB-evolution, when the mass-loss rate increases by a factor of 10-100. By their different optical depths, the three dust shells studied here may represent different stages of the “superwind” and different initial masses.

Key words. Techniques: interferometric – Stars: AGB and post-AGB – Stars: late-type – Stars: circumstellar matter

1. Introduction

OH/IR stars are medium-mass, highly evolved objects, which either have nearly reached the tip of the asymptotic giant branch (AGB) or may just have left the AGB toward the post-AGB stage. Observational characteristics are an infrared excess and the presence of hydroxyl (OH) masers, as well as variability due to the release of cool, dust-driven winds with a high mass-loss rate (“superwind”), prior to forming a planetary nebula (PN). These critical, late phases are of fundamental interest to a complete understanding of stellar evolution.

Mass-loss rates of stars at the tip of the AGB can reach values of up to $\sim 10^{-4} M_{\odot} \text{ yr}^{-1}$ (De Beck et al. 2010). Such a “superwind” can expel a considerable fraction of the stellar mass in a relatively short time ($< 100\,000$ years). Time-dependent, dust-driven wind models (Wachter et al. 2002; Mattsson et al. 2010) reproduce such mass-loss rates reasonably well for carbon-rich AGB stars. A pulsating photosphere for the initial mechanical

energy input and low effective temperatures lead to conditions favorable for dust formation in the denser regions of such a circumstellar envelope (CSE). Due to their high absorption coefficient, carbon dust grains are accelerated by the stellar radiation such that the star is eventually surrounded by an expanding envelope. It significantly changes the spectral appearance of the central star, due to its large optical depth at visual and near-IR wavelengths and thermal re-emission in the farther IR. Except for the case of the dust-enshrouded Mira variable IRC -20197 (Jeong et al. 2003), such self-consistent wind models do not yet exist for oxygen-rich AGB stars, and, moreover, recent studies by Woitke (2006) and Höfner & Andersen (2007) indicated fundamental problems in our understanding of the wind-driving mechanism for oxygen-rich AGB stars due to an insufficient radiation pressure on silicate grains.

However, previous high spatial resolution work on OH/IR stars confirmed the presence of circumstellar dust shells of large optical depth for oxygen-rich stars near the tip of the AGB. *K*-band speckle interferometry of the OH/IR star OH 104.9+2.4 (Riechers et al. 2004) measured a circumstellar dust shell of

[★] Based on observations made with the ESO VLT Interferometer at the La Silla Paranal Observatory under programme ID 081.D-0325.

Table 1. Characteristics of the sources

| IRAS Name | K | $J - K$ | $K - L$ | D (kpc) | S_{OH} (Jy) | v_{exp} (km s $^{-1}$) |
|------------|------|---------|---------|------------|-------------------------|-------------------------------------|
| 13479-5436 | 4.89 | 4.39 | 2.15 | 2.9 | 0.68 | 17.7 |
| 14086-6907 | 4.27 | 3.28 | 1.98 | 2.4 | 6.15 | 13.4 |
| 17020-5254 | 4.15 | 2.59 | 1.38 | 2.5 | 1.08 | 13.4 |

large optical depth of 6.5 at $2.2\,\mu\text{m}$ with an apparent angular diameter of 47 ± 3 mas (FWHM), corresponding to 112 ± 13 AU. Chesneau et al. (2005) resolved the mid-IR dusty envelope of the OH/IR star OH 26.5+0.6 to a FWHM size of $286\text{ mas} \times 214\text{ mas}$, or about $390\text{ AU} \times 290\text{ AU}$. Size and complexity of the circumstellar structures of OH/IR stars narrate the mass-loss history of the final AGB stages, which in turn shapes the future planetary nebula. The recent development of very high angular resolution instrumentation has finally enabled us to decipher this crucial evidence.

In this research note, we study the three OH/IR stars IRAS 13479-5436, IRAS 14086-6907 and IRAS 17020-5254. All three objects exhibit a typical two-peak maser profile at 1612 MHz (te Lintel Hekkert et al. 1991), which is indicative of an expanding CSE. Furthermore, a large infrared excess and a strong $9.7\,\mu\text{m}$ silicate emission feature in the mid-IR spectra indicate the presence of an optically thick, dust-rich CSE. Table 1 shows the near-infrared photometry and colors of Fouqué et al. (1992), the bolometric distances given by Lepine et al. (1995), the average flux densities S_{OH} at 1612 MHz between the two OH maser peaks, and the respective expansion velocities v_{exp} of the OH shells according to te Lintel Hekkert et al. (1991).

2. Observations and Data Reduction

We obtained near-infrared H - and K -band spectro-interferometric observations of the three OH/IR stars IRAS 13479-5436, IRAS 14086-6907, and IRAS 17020-5254, using the AMBER instrument (Petrov et al. 2007) of the VLT Interferometer (VLTI) in low resolution mode ($R \sim 35$) and three of the 1.8 m Auxiliary Telescopes (AT). These were positioned on stations E0, G0 and H0, providing ground baselines of 16 m, 32 m and 48 m, along the same ground position angle of -109° East of North. The AMBER low resolution data also include coverage of the J band, but because of low J -band fluxes and, hence the poor quality of the respective visibility data, we were unable to include the J -band in our study.

Because our target stars are dust-enshrouded objects, they have V magnitudes too faint to use them as Coudé guide stars. Instead, we resorted to the off-axis guide-star option of the VLTI and chose the stars GSC 0866800251, GSC 0924401731, and GSC 0872601051 from the HST Guide Star Catalog II (Lasker et al. 2008). These guide stars are located at distances of 42 arcsec, 39 arcsec, and 55 arcsec, respectively, from our target stars listed above. The external VLTI fringe tracker FINITO was not used. The AMBER detector integration time (DIT) was set at 0.1 sec. After each target a calibration star of well known diameter from the catalog of Mérand et al. (2005) was observed (HD 126284 with $\Theta_{\text{UD}} = 1.14 \pm 0.02\text{ mas}$, HD 114912 with $\Theta_{\text{UD}} = 0.95 \pm 0.01\text{ mas}$, and HD 154486 with $\Theta_{\text{UD}} = 1.06 \pm 0.02\text{ mas}$). The observations presented here were all obtained on 4 April 2008. Table 2 summarizes the observational details.

Data reduction was performed with standard procedures offered by the *amdlb* 3.0.3 package, as provided by the AMBER consortium and the Jean-Marie Mariotti Center (Tatulli et al.

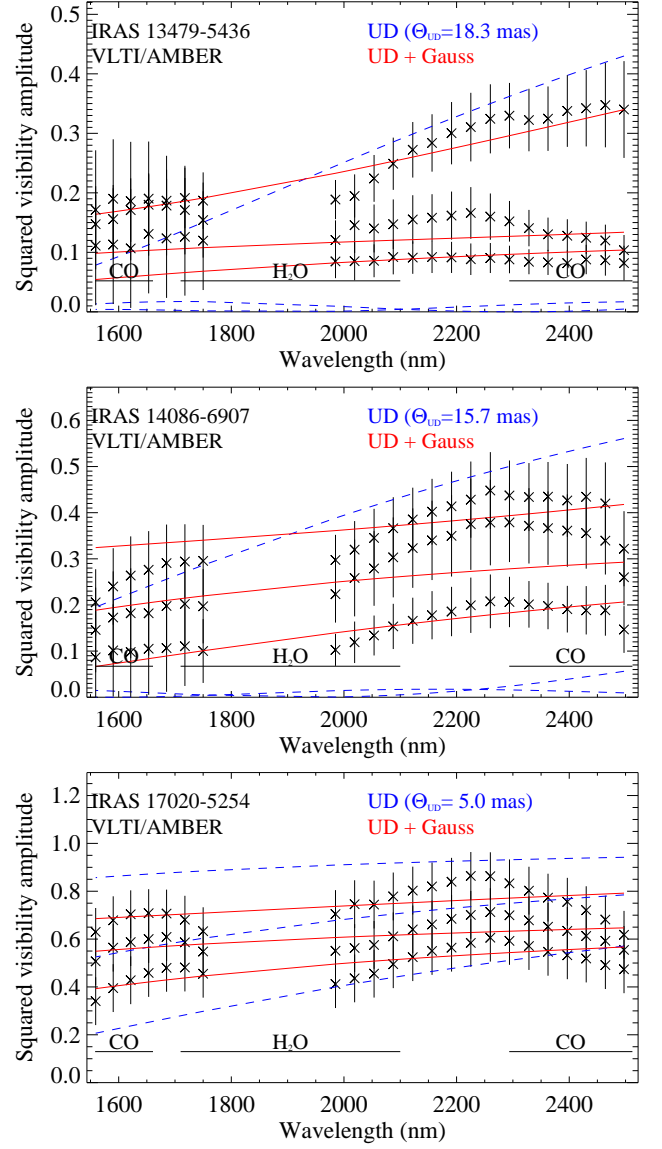


Fig. 1. Squared visibility amplitudes as a function of wavelength of IRAS 13479-5436, IRAS 14086-6907, and IRAS 17020-5254 (from top to bottom). The position of H_2O and CO bands are indicated. The blue dashed lines show the best-fit of a single component uniform disk model. The red solid lines indicate the best-fit two-component model consisting of a uniform disk describing the central source and a Gaussian disk describing the circumstellar dust shell. The fit parameters of the two-component model are indicated in Tab. 3. In each panel, the three sets of lines correspond to baselines (from top to bottom) E0-G0, G0-H0, E0-H0 with increasing projected baseline lengths as listed in Tab. 2.

2007; Chelli et al. 2009). The wavelength scale was corrected by a scaling-factor of 1.03 and a linear offset of $-0.14\,\mu\text{m}$. These parameters were obtained by a comparison of the observed flux distribution of the calibrators with a synthetic flux curve as in Wittkowski et al. (2011). The synthetic flux curve includes the telluric spectrum, the stellar spectrum, and transmission curves of optical components of AMBER. Visibility spectra were obtained by using an average of the two transfer function measurements, which were taken closest in time to the science target measurements. Fig. 1 shows the resulting visibility data as a function of wavelength and Fig. 2 shows the same visibility data

Table 2. Observation log of 4 April 2008

| Target | R.A | Dec | Starting time | Category | Projected baseline (m) | P.A. (deg) | Seeing (arcsec) |
|-----------------|------------|-----------|---------------|------------|---------------------------|---------------|--------------------|
| IRAS 13479-5436 | 13 51 12.6 | -54 51 13 | 05:15:18.650 | Science | 15.89/31.76/47.65 | -110 | 0.83 |
| HD 126284 | 14 26 22.2 | -55 15 33 | 05:39:33.025 | Calibrator | | | 1.01 |
| IRAS 14086-6907 | 14 12 50.5 | -69 21 10 | 06:05:21.233 | Science | 15.49/30.97/46.47 | -100 | 0.86 |
| HD 114912 | 13 15 25.5 | -69 40 45 | 06:33:44.509 | Calibrator | | | 1.47 |
| IRAS 17020-5254 | 17 06 00.7 | -52 58 47 | 06:58:34.476 | Science | 15.92/31.83/47.76 | -128 | 0.96 |
| HD 154486 | 17 08 08.2 | -48 53 01 | 07:24:43.020 | Calibrator | | | 0.95 |

Table 3. Fit results of the two-component model

| IRAS | 13479-5436 | 14086-6907 | 17020-5254 |
|-----------------|-----------------|-----------------|-----------------|
| UD diam. [mas] | 4.2 ± 0.6 | 5.4 ± 0.4 | 3.2 ± 0.4 |
| CSE, FWHM [mas] | 18.1 ± 0.9 | 25.2 ± 4.4 | 17.1 ± 3.3 |
| % flux of UD | 0.39 ± 0.02 | 0.62 ± 0.03 | 0.84 ± 0.02 |
| % flux of CSE | 0.61 ± 0.02 | 0.38 ± 0.03 | 0.16 ± 0.02 |

as a function of spatial frequency, together with visibility models discussed below in Sect. 3.

3. Modeling the Visibility Function

As a first approach to describe the visibility data, we used a fit of a single uniform disk (UD). A single-component model would be expected for either a stellar source that does not show a significant near-IR CSE, or for an optically thick CSE that completely obscures the central stellar source. The formally best-fitting curves are indicated in Figs. 1 & 2 by the dashed blue lines. Compared to the visibility data, these curves clearly illustrate that a single-component model can not provide a good description of our sources. In particular, a single-component model can not explain the comparable small differences of the visibility data for different baseline lengths.

We then used a simple geometrical two-component model of a UD representing the central stellar source and a Gaussian disk representing the dusty CSE. The free parameters of this two-component model are the angular diameter of the UD, the FWHM of the Gaussian disk, and the flux ratio between these two components. Following Dyck (2000) and Berger & Segransan (2007), let θ_{UD} be the angular diameter of the central UD, θ_{Gauss} the FWHM of the Gaussian disk, and V_p the fraction of the flux contributed by the UD, i.e. the fraction of the attenuated stellar flux shining through the dusty envelope. The visibility amplitude $V(s)$ as a function of spatial frequency s is then given by:

$$V(s) = V_p \left[\frac{2 J_1(\pi \theta_{UD} s)}{\pi \theta_{UD} s} \right] + (1 - V_p) \left[\exp \left(-\frac{(\pi \theta_{Gauss} s)^2}{4 \ln 2} \right) \right] \quad (1)$$

where J_1 is the first-order Bessel function of the first kind. A satisfactory fit to the visibilities was obtained using a Levenberg-Marquardt least-squares minimization algorithm. The best-fit parameters of the two-component model are listed in Table 3. Because we use all spectral channels in the fit procedure, the resulting values are near-IR values averaged over the *H*- and *K*-bands. The best-fit curves are indicated by the red solid lines in Figs. 1 & 2. These curves indicate that the two-component model provides a good description of the overall shape of the visibility curves of all three sources.

In comparison to the two-component model, the measured visibility data of all three sources show additional wavelength-dependent features that are not explained by our simple UD

model with wavelength-independent diameter. The visibility values show local maxima near wavelengths of $2.2 \mu\text{m}$ in the *K*-band and near $1.7 \mu\text{m}$ in the *H*-band, and decreasing visibility values toward the edges of the *H* and *K* bands. The decrease of the visibility values coincides with the positions of H_2O and CO molecular bands, as indicated in Fig. 1. These visibility features resemble those that have previously been detected in AMBER data of several Mira variable AGB stars (Witkowski et al. 2008, 2011), of the super-giant or super-AGB star VX Sgr (Chiavassa et al. 2010), and of the semi-regular AGB star RS Cap (Martí-Vidal et al. 2011). These visibility features were interpreted as being indicative of molecular layers, in the near-IR most importantly H_2O and CO , lying above the continuum-forming photosphere. In other words, this means that our simple UD model of the central stellar source could further be sub-divided into a wavelength-independent photospheric continuum diameter and a close atmospheric molecular shell with wavelength-dependent molecular opacity. The presence of the same features in the AMBER data of all three OH/IR stars of our sample confirms that atmospheric molecular layers are a common phenomenon among AGB stars of very different luminosities and mass-loss rates, alike. We note that the best-fit UD diameters listed in Tab. 3 are then expected to overestimate the continuum photospheric radii, as a result of the additional intensity contribution by the atmospheric molecular layers at larger radii. For less evolved AGB stars, this overestimate may amount to up to about 30%, depending on the stellar phase (Ireland et al. 2004).

Ideally, of course, we should match the visibility data with synthetic visibilities derived from physical models of OH/IR stars. However, consistent dynamic model atmosphere and wind models are not yet available for oxygen-rich AGB stars, except for the attempt by Jeong et al. (2003). Also, dust-free dynamic model atmospheres do not exist for the stellar parameters of OH/IR stars exhibiting luminosities above $10\,000 L_\odot$ and effective temperatures below 2000 K (Lepine et al. 1995), so that approaches of a combination of dust-free dynamic model atmospheres with radiative transfer models of the dust shell can not be attempted (as performed for Mira variable AGB stars by Witkowski et al. 2007; Karovicova et al. 2011). This means as well that our fit results of the two-component model in Tab. 3 are only indicative of the general characteristic dimensions of the central stellar component and the dust shell, but do not provide accurate radius determinations of certain layers.

4. Results

We here summarize the best-fit parameters of the above-mentioned two-component model. In order to estimate absolute sizes of the central stellar component, including the continuum-forming layers and overlying molecular layers, and the outer circumstellar dust shells, we rely on the bolometric distances given

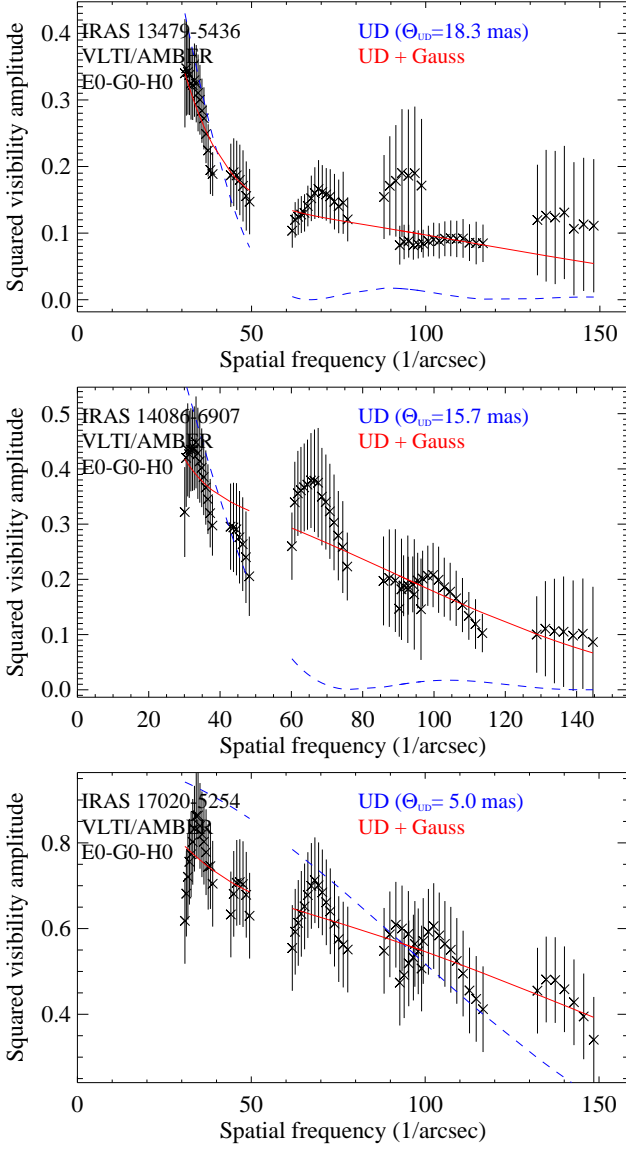


Fig. 2. Squared visibility amplitudes as a function of wavelength of IRAS 13479-5436, IRAS 14086-6907, and IRAS 17020-5254 (from top to bottom). The blue dashed lines show the best-fit of a single component uniform disk model. The red solid lines indicate the best-fit two-component model consisting of a uniform disk describing the central source and a Gaussian disk describing the circumstellar dust shell. The fit parameters of the two-component model are indicated in Tab. 3.

by Lepine et al. (1995) (see Table 1), albeit their uncertainties may amount to up to a factor of two.

IRAS 13479-5436: The best-fit visibility model consists of a CSE with Gaussian FWHM of 18.1 ± 0.9 mas plus a central UD of 4.2 ± 0.6 mas in diameter. The UD contributes 39% of the observed near-IR flux of this object. The angular scales correspond to a near-IR FWHM of the CSE of $\sim 11300 R_{\odot}$ or ~ 53 AU and a radius of the central stellar disk of $\sim 1300 R_{\odot}$. For comparison, the calibration of the stellar radius as a function of $K - L$ color by Lepine et al. (1995) gives a stellar radius of $\sim 1700 R_{\odot}$. The rather small contribution from the stellar UD disk, as well as the infrared colors (largest $J - K$ color in Table 1), indicate a large optical depth of the CSE.

IRAS 14086-6907: The best-fit visibility model consists of a CSE with Gaussian FWHM of 25.2 ± 4.4 mas plus a central UD of 5.4 ± 0.4 mas in diameter, which contributes 62% of the total flux. The corresponding FWHM of the CSE is $\sim 13000 R_{\odot}$ or ~ 60 AU, and the radius of the central UD is $\sim 1400 R_{\odot}$. For comparison, the $K - L$ calibration by Lepine et al. gives a stellar radius of $\sim 1500 R_{\odot}$. In terms of both, stellar flux contribution and $J - K$ color, this object consistently takes the place between the other two.

IRAS 17020-5254: The best-fit visibility model consists of a CSE with Gaussian FWHM of 17.1 ± 3.3 mas plus a central UD of 3.2 ± 0.4 mas in diameter, contributing 84% of the total flux. The corresponding FWHM of the CSE is $\sim 9000 R_{\odot}$ or ~ 43 AU, and the radius of the central UD is $\sim 860 R_{\odot}$ (compared to $\sim 912 R_{\odot}$ derived from the $K - L$ calibration). The large flux contribution from the stellar disk, as well as the small value of $J - K = 2.4$, both indicate that we see mostly the stellar disk including atmospheric molecular layers, with a comparably small contribution from a diluted, fairly transparent dust-envelope.

Please note that there is a consistent and, hence, convincing relation between (larger) IR-colors and (larger) flux contribution from the dust-rich CSE of these three objects.

5. Discussion

From computations of hydrodynamical wind models of long-period variables (Winters et al. 2000) we derived CSE radii, as they would appear in the near IR, to compare to the observed values. Although the models available to us are based on a carbon-rich chemistry, we nevertheless consider this comparison to be of some relevance, given that both types of objects, C-rich and O-rich dust-enshrouded stars with large IR excess, are located at the tip of the AGB. In particular, we are interested in whether the dimensions in the O-rich case compare with those of the C-rich case, although the details of the wind driving mechanisms are expected to be different. We should also note that the uncertain distances already give this comparison a very approximate character.

The above wind models apply grey radiative transfer and consequently the resulting radii do not depend on wavelength. They vary in time, though, due to the stellar pulsation (prescribed by a piston approach for the inner boundary condition). Each wind model is characterized by a set of the stellar parameters mass M , luminosity L , effective temperature T_e , as well as by the carbon-to-oxygen ratio C/O of the atmospheric chemical composition and pulsation parameters period P and velocity amplitude Δv of the piston. Mass-loss rates have been determined by averaging typically over 20 periods.

As representative cases we selected two models (w69 and w63, see row no. 52 and 23 of Table 3 in Wachter et al. 2002) showing mass-loss rates of 1.8 and $5.0 \times 10^{-5} M_{\odot} \text{ yr}^{-1}$, respectively. The stellar parameters are masses of 1.0 and $0.8 M_{\odot}$, temperatures of 2800 and 2600 K, respectively, and a luminosity (both) of $L = 10000 L_{\odot}$. The other parameters are, in both cases, C/O = 1.3, $P = 640$ d, and $\Delta v = 5 \text{ km s}^{-1}$. The observable CSE diameter of the first model (with the lower mass-loss rate) varies between approximately 2000 and 6000 solar radii over several pulsation cycles. The second model (with the higher mass-loss rate) has a diameter between about $5000 R_{\odot}$ and $9000 R_{\odot}$. With values between $9000 R_{\odot}$ and $13000 R_{\odot}$ the observationally determined FWHM of the CSE of our OH/IR stars are larger than the CSE diameters of these models but generally of similar extension. The model radii based on the adopted stellar luminosity and effective temperatures vary between 340 – $520 R_{\odot}$ and be-

tween $400\text{--}600R_{\odot}$, and are also smaller than our best-fit UD radii and smaller than those derived from the $K - L$ calibration by Lepine et al. (1995). These differences may be due to different stellar parameters and/or an overestimate of the stellar radius because of the presence of molecular layers as discussed in Sect. 3.

From the 1612 MHz observations (te Lintel Hekkert et al. 1991) we know the expansion velocities of the OH maser shells. Here, the value of $v_{\text{exp}} = 17.7\text{ km s}^{-1}$ for IRAS 13479-5436 is larger than those of IRAS 14086-6907 and IRAS 17020-5254 (See Table 1). Given that the stellar luminosities are thought to increase with increasing OH expansion velocities (e.g., Sevenster 2002), IRAS 13479-5436 would have a higher luminosity than the other two sources, which is also consistent with its largest $K - L$ color index and the calibration by Lepine et al. (1995). Also, Baud & Habing (1983) developed a relation between the main sequence mass and the OH outflow velocity of $\log(M/M_{\odot}) = (v_{\text{exp}} - 8)/16$, suggesting the same main sequence mass of $\sim 2M_{\odot}$ for IRAS 14086-6907 and IRAS 17020-5254 and a larger main sequence mass of $\sim 4M_{\odot}$ for IRAS 13479-5436 together with its higher luminosity.

Additionally, the calibrations by Lepine et al. (1995) as a function of color index indicate an increasing optical depth of the CSE of OH/IR stars with increasing $K - L$ color index, which is supported by our observations (see Sect. 3). A larger optical depth of the CSE indicates a larger integrated mass-loss history of the star. The wind models by Wachter et al. (2002), which are coupled to a stellar evolutionary code, indicate that the maximum mass-loss rate increases with initial mass, and that the shape becomes more spiky towards the end. Altogether we may speculate that the larger optical depth of the CSE of IRAS 13479-5436 compared to the other two sources may be a result of a higher initial mass and an evolutionary phase very close to the tip of the AGB evolution and thus the spike of the mass-loss rate. The different optical depths of the CSEs of IRAS 14086-6907 and IRAS 17020-5254, which have similar expansion velocities, may then rather be caused by an earlier evolutionary phase of IRAS 17020-5254 compared to IRAS 14086-6907 along the same initial mass track. Accordingly, IRAS 17020-5254 could even be an intermediate object, lying between a Mira-variable and a tip-AGB star.

6. Conclusions

Using the VLTI/AMBER instrument, we determined angular diameters for the three OH/IR stars IRAS 13479-5436, IRAS 14086-6907 and IRAS 17020-5254 and their CSEs. Even though our visibility fits are based on a simple two-component geometrical model, they provide characteristic radial dimensions of the stars and their dust-rich shells, as well as constraints on the relative flux contributions from these different components.

Our near-IR visibility data also indicate wavelength-dependent features, which resemble those detected in earlier AMBER observations of semi-regular and Mira-variable AGB stars, which are correlated with the positions of H_2O and CO bands, and which are interpreted as the result of atmospheric molecular layers lying above the continuum-forming photospheres. This result confirms that atmospheric molecular layers are a common phenomenon among AGB stars of very different luminosities and mass-loss rates, alike.

We also confirm that the circumstellar dust shells contribute significantly to the near-IR flux of our sources, unlike in the case of Mira variable AGB stars, which can well be described by dust-free model atmospheres at near-IR wavelengths

(e.g. Woodruff et al. 2004; Fedele et al. 2005; Wittkowski et al. 2008). This indicates a large optical depth of the CSE, which we interpret as the result of the “superwind” phase, the final 10 000 to 30 000 years of AGB evolution, when the mass-loss rate increases by a factor of 10-100. This result also observationally confirms that oxygen-rich AGB stars develop a similar “superwind” as carbon-rich AGB stars, although their wind-driving mechanisms are not yet understood to the same detail.

Even though the three stars have the same classification, interestingly they show somewhat different characteristics. This could be attributed to their different initial masses and slightly different stages of evolution.

Acknowledgements. This research has benefited from the AMBER data reduction package of the Jean-Marie Mariotti Center¹, and the SIMBAD database, operated at CDS, Strasbourg, France. We gratefully acknowledge support by CONACyT, Mexico and the ESO Headquarters in Garching under their studentship programmes (ARV), and by PROMEP, Mexico, project 103.5/10/4684 (AW).

References

- Baud, B. & Habing, H.J. 1983, *A&A*, 127, 73
- De Beck, E., Decin, L., de Koter, A., et al. 2010, *A&A*, 523, A18
- Berger, J. P. & Segransan, D. 2007, *New Astronomy Reviews*, 51, 576
- Chelli, A., Utrera, O. H., & Duvert, G. 2009, *A&A*, 502, 705
- Chesneau, O., Verhoelst, T., Lopez, B., et al. 2005, *A&A*, 435, 563
- Chiavassa, A., Lacour, S., Millour, F., et al. 2010, *A&A*, 511, A51
- Dyck, H. M. 2000, *Interferometry with Two Telescopes*, in *Principles of Long Baseline Stellar Interferometry*, ed. P. R. Lawson (Jet Propulsion Laboratory), 194
- Fedele, D., Wittkowski, M., Parece, F., et al. 2005, *A&A*, 431, L77
- Fouqué, P., Le Bertre, T., Epchtein, N., Guglielmo, F., & Kerschbaum, F. 1992, *A&AS*, 93, 151
- Ireland, M. J., Scholz, & Wood, P. 2004, *MNRAS*, 367, 1585
- Höfner, S., & Andersen, A. C. 2007, *A&A*, 465, L39
- Jeong, K. S., Winters, J. M., Le Bertre, T., & Sedlmayr, E. 2003, *A&A*, 407, 191
- Karovicova, I., Wittkowski, M., Boboltz, D. A., et al. 2011, *A&A*, 532, A134
- Lasker, B. M., Lattanzi, M. G., McLean, B. J., et al. 2008, *AJ*, 136, 735
- Lepine, J. R. D., Ortiz, R., Epchtein, N. 1995, *A&A*, 299, 453
- Martí-Vidal, I., Marcaide, J. M., Quirrenbach, A., et al. 2011, *A&A*, 529, A115
- Mattsson, L., Wahlin, L., & Höfner, S. 2010, *A&A*, 509, A14
- Mérand, A., Bordé, P. & Coudé du Foresto, V. 2005, *A&A*, 433, 1155
- Petrov, R.G., Malbet, F., Weigelt, G., et al. 2007, *A&A*, 464, 1
- Riechers, D., Balega, Y., Driebe, T., et al. 2004, *A&A*, 424, 165
- Sevenster, M. N. 2002, *AJ*, 123, 2772
- Tatulli, E., Millour, F., Chelli, A., et al. 2007, *A&A*, 464, 29
- te Lintel Hekkert, P., Caswell, J. L., Habing, H. J., et al. 1991, *A&AS*, 90, 327
- Wachter, A., Schröder, K.-P., Winters, J. M., Arndt, T. U., & Sedlmayr, E. 2002, *A&A*, 384, 452
- Winters, J.M., Le Bertre, T., Jeong, K.S., Helling, Ch., & Sedlmayr, E., 2000, *A&A*, 361, 641
- Wittkowski, M., Boboltz, D. A., Ohnaka, K., et al. 2007, *A&A*, 470, 191
- Wittkowski, M., Boboltz, D. A., Driebe, T., et al. 2008, *A&A*, 479, L21
- Wittkowski, M., Boboltz, D. A., Ireland, M., et al. 2011, *A&A*, 532, L7
- Woitke, P. 2006, *A&A*, 452, 537
- Woodruff, H. C., Eberhardt, M., Driebe, T., et al. 2004, *A&A*, 421, 703

¹ Available at <http://www.jmmc.fr/amberdrs>